Accepted Manuscript

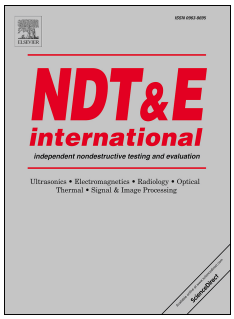

High power phased EMAT arrays for nondestructive testing of As-cast steel

Jozef Tkocz, David Greenshields, Steven Dixon

PII: S0963-8695(18)30409-2

DOI: https://doi.org/10.1016/j.ndteint.2018.11.001

Reference: JNDT 2043

To appear in: *NDT and E International*

Received Date: 20 July 2018

Revised Date: 2 November 2018

Accepted Date: 2 November 2018

Please cite this article as: Tkocz J, Greenshields D, Dixon S, High power phased EMAT arrays for nondestructive testing of As-cast steel, *NDT and E International* (2018), doi: https://doi.org/10.1016/j.ndteint.2018.11.001.

High Power Phased EMAT Arrays for Nondestructive Testing of As-Cast Steel

Jozef Tkocz[a,*], David Greenshields[a], Steven Dixon[a]

[a]*Department of Physics, University of Warwick, Coventry, CV4 7AL, United Kingdom*

Abstract

A new high-power electromagnetic acoustic transducer (EMAT) solid state pulser system has been developed that is capable of driving up to 4 EMAT coils with programmable phase delays, allowing for focusing and steering of the acoustic field. Each channel is capable of supplying an excitation current of up to 1.75 kA for a pulse with a rise time of 1 μs. Finite element and experimental data are presented which demonstrate a signal enhancement by a factor of 3.5 (compared to a single EMAT coil) when using the system to transmit a longitudinal ultrasound pulse through a 22.5 cm thick as-cast steel slab sample. Further signal enhancement is demonstrated through the use of an array of detection EMATs, and a demonstration of artificial internal defect detection is presented on a thick steel sample. The design of this system is such that it has the potential to be employed at elevated temperatures for diagnostic measurements of steel during the continuous casting process.

Keywords: EMAT, ultrasonics, array, longitudinal wave

1. Introduction

Diagnostic assessment of internal product quality during the continuous casting of steel is currently limited to offline and largely destructive methods, such as acid etching followed by sulphur printing [1], chemical analysis of drilled core samples [2] and optical emission spectroscopy methods [3]. There is a

*Corresponding author
Email address: j.tkocz@warwick.ac.uk (Jozef Tkocz)

requirement from industry to perform product quality tests non-destructively and continuously during the casting process to allow feedback to the casting operators. This could, in principle, mitigate the development of internal defects, which both reduce the steel's sale value and in some cases present safety concerns [2, 4, 5].

Detection of internal defects during the casting process presents a number of difficulties for conventional non-destructive evaluation (NDE) techniques; the high operating temperatures, surface roughness and continuous movement of the sample necessitate the consideration of a non-contacting approach. The thickness of a cast steel slab lies in a range from 12 - 30 cm, which is sufficient to preclude the consideration of practical radiographic measurements, and to perform active thermography through such a sample thickness would be impractical, due to the variable and uncontrolled ambient temperatures of the casting environment and the likelihood of false indications arising from surface oxide scale. Ultrasound measurements have been identified as a realistic prospect of probing the surface and bulk of a cast slab and are the subject of previous studies on cast steel diagnostics [6, 7, 8, 9], but there still exist a number of challenges when attempting to use acoustics. Namely, the slab itself is relatively thick (up to 30 cm) and contains inhomogeneous and relatively large grain structures when compared to the expected dimensions of a casting defect. Hence attenuation of ultrasound signals, in particular the higher-frequency signals that have scattered from defects, will reduce detected signal amplitudes significantly. Additionally, previous studies have demonstrated that ultrasonic attenuation in metallic samples increases at high temperatures [7, 10, 11].

Non-contacting methods of ultrasound generation are well-established [12, 13, 14, 15], but the problem of non-contact measurements during continuous casting requires special considerations. The high sample temperatures of up to 1100 °C potentially make water jet coupling of piezoelectric transducers impractical [16], and the large impedance mismatch between the air and the steel sample precludes the use of air-coupled transducers [14]. Ablative laser generation of ultrasound in steel billets during the casting process has already been

demonstrated, and generates sufficient ultrasound wave amplitudes for both surface defect characterisation and possibly bulk wave measurements [8, 17, 18]. However, laser sources are relatively expensive, high-power laser beams present implications for the steel mill's safety regulations, the surface ablation pits can interfere with other visual inspection systems in place at the steel mill and large surface coverage interferometric detection of ultrasound waves using lasers is difficult in optically-rough and moving samples [19]. Electromagnetic acoustic transducers (EMATs) have been used as ultrasonic detectors in conjunction with ablative laser generation sources for surface measurements of continuously cast steel billets [8, 20], and so represent one possibility for performing bulk diagnostic tests. The low cost and minimal requirement for adaptations to the steel mill's safety protocols makes an entirely EMAT-based system attractive, but their poor transduction efficiency presents challenges in obtaining a practicable signal-to-noise ratio [21, 22]. The work presented here concerns the development of an EMAT phased array concept to overcome this inherent drawback of EMATs.

2. Methods

2.1. EMAT Generation and Detection

The EMAT generator devices presented in this work consist of an inductor coil driven with a high amplitude (kA) dynamic current. Such devices have been demonstrated in previous studies to be relatively efficient bulk wave generation sources [23, 24, 25, 26], and should in principle be more industrially-robust than conventional EMAT designs, since there is no requirement for an electromagnet or for active cooling of a permanent magnetic material to maintain a sensor temperature lower than the Curie point.

When a coil-only EMAT above an electrically-conducting sample is driven with a large transient current pulse, the resulting time-varying magnetic field induces an eddy current density profile in the sample. Under the plane wave approximation for the magnetic field, the magnitude and phase of this current

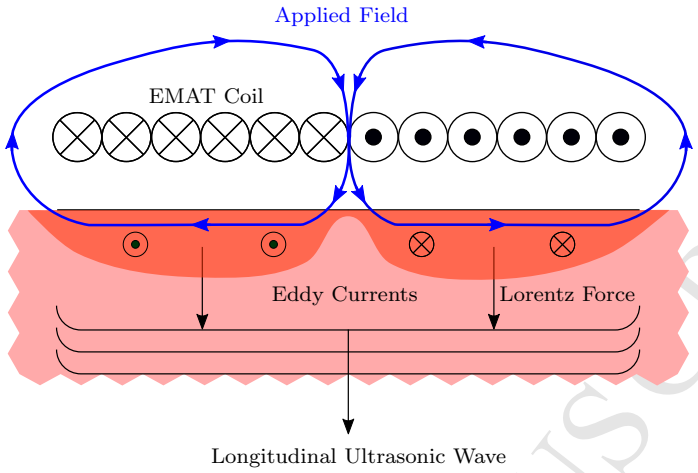

Figure 1: Schematic diagram of a coil-only EMAT generator. The dynamic driving current in the coil leads to a time-varying magnetic field, which induces eddy currents in the sample surface. These eddy currents interact with the dynamic field to produce mechanical forces in accordance with equation 2, and hence lead to the propagation of ultrasound waves.

density profile decays exponentially with depth into the sample with a characteristic length scale known as the electromagnetic skin depth [27, 28, 29]:

$$\mathbf{J} = \mathbf{J}_0 e^{-i\frac{z}{\delta}} e^{-\frac{z}{\delta}}, \tag{1}$$

where $\mathbf{J}_0$ is the magnitude of the current density, $\mathbf{J}$, at the surface, z is the depth into the sample and δ is the electromagnetic skin depth. The total induced current, as calculated from an integration of the current density profile over depth, can be shown to be equivalent to a surface image current with magnitude $\frac{\mathbf{J}_0\delta}{2}$ and a phase lag with respect to the driving voltage of $\frac{-\pi}{4}$ [27], allowing the eddy current distribution to be modeled as a current sheet as shown in figure 1.

The eddy currents interact with the EMAT's dynamic field and induce mechanical forces in the sample's surface through the Lorentz force ($\mathbf{F}_L$), which is a vector cross product of the eddy current density and the magnetic field density ($\mathbf{B}$) [29]:

$$\mathbf{F}_L = \mathbf{J} \times \mathbf{B}. \tag{2}$$

Inspection of figure 1 indicates that the polarity of both the induced eddy cur-

rents and the dynamic field lines will reverse when the current in the driving coil is reversed, leading to exclusively repulsive mechanical forces normal to the sample surface at twice the frequency of the applied driving current [29].

EMAT generation relies on the scattering of conduction band electrons from metal atoms to impart momentum into the metallic lattice; this is an inefficient process, due to the small electron-atom mass ratio. This contrasts with EMAT detection, which is a more efficient process, since sample motion is inherent to the incidence of an acoustic wave. The motion of the conducting sample in an applied magnetic field induces dynamic currents in the sample, which themselves induce a measurable potential difference in the detection coil. In detection, a static bias magnetic field is always required, usually supplied by a permanent magnet [29]. This usually means that a coil-only EMAT cannot act as a detector (work has been published which demonstrates the use of a specialised driving circuit for coil-only devices to detect bulk ultrasonic modes [24], but due to the added complexity, such a setup is not considered here).

The inherent inefficiency of electromagnetic ultrasound generation means that EMAT measurements typically suffer from poor signal-to-noise ratios. This issue is compounded by the expected low signal amplitudes arising from the cast steel sample grain coarseness and high temperatures discussed in section 1, and hence design considerations are required to improve the signal amplitude of an EMAT-based system.

2.2. Phased Array Generation and Beamforming

One approach that can be taken to improve the signal-to-noise ratio of a measurement is to utilise a phased array to increase the signal amplitude through linear superposition; if the ultrasound signals are summed coherently, the resulting total signal amplitude increases, whilst any stochastic noise in the measurement sums incoherently. Enhancement of EMAT sensitivity by the geometric focusing of shear waves has been reported previously, however the approach taken relied on toneburst current excitations, which are more limited in power than the pulsed currents described in this work, and the dependence on geo-

metric focusing prevented dynamic beamforming [30, 21]. The novelty of the work described here is the development of a high power EMAT phased array, designed specifically for the inspection of thick, attenuative industrial samples.

Phased array generation and detection of ultrasound is a well-established technique for focusing and steering acoustic waves in both medical diagnostics and NDE [31]. By applying appropriate phase delays to each element, a point in space can be chosen such that the wavefront from each element will arrive simultaneously so that the acoustic beam is locally intense. In order to perform beam focusing, the phase delays are calculated by first calculating the propagation time from each element to the chosen focus, then subtracting the maximum propagation time from each element. The applied time delay, ϕ, can be expressed as:

$$\phi_i = \frac{\sqrt{x_{max}^2 + y_{max}^2}}{c_L} - \frac{\sqrt{x_i^2 + y_i^2}}{c_L}, \tag{3}$$

where the subscript i refers to the i^{th} element in the array, c_L is the longitudinal wave propagation speed, x is the displacement in x of the element from the focus, y is the displacement in y from the focus and the subscript max refers to the element that lies at the greatest distance from the focus.

The work presented here describes the development of a phased EMAT array generation system to enhance signals transmitted through the full thickness of as-cast steel slab samples.

3. Results

3.1. EMAT Phased Array Driving Electronics

As discussed in section 2.1, coil-only EMAT designs require large dynamic currents for efficient ultrasound generation, and hence a bespoke excitation circuit. The driving electronics for the experimental tests of the EMAT generation array consist of a capacitor bank discharged through a solid state switching device for each channel (see figure 2). The phase delays are applied by a field-programmable gate array (FPGA) unit and have a temporal resolution of 2.5 ns. The temporal current profile of the excitation pulse was measured by placing a

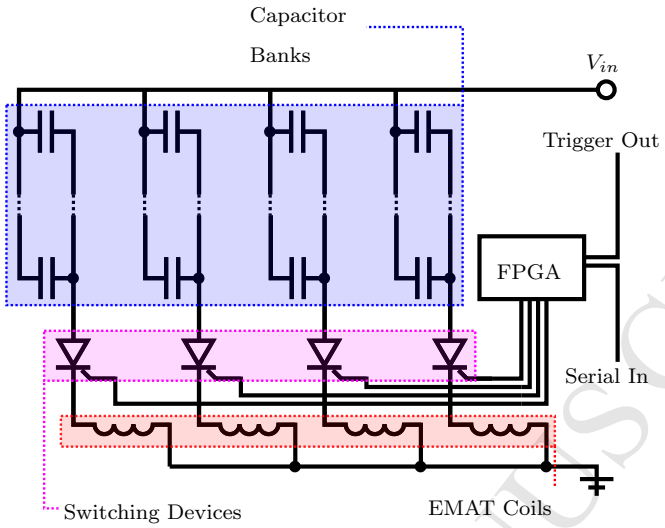

Figure 2: Schematic diagram of the phased array driving circuit. Each channel consists of a bank of capacitors that are charged to an input voltage, V_{in} = 850 V. For each channel, a solid state switching device is used to discharge the capacitor bank's current through the EMAT coils. A field-programmable gate array (FPGA) unit is used to apply phase delays on each channel, with the phase delays pre-determined on a personal computer and sent to the FPGA unit over a serial connection.

small resistance of 0.1 Ω in series with the EMAT coil being driven. A voltage measurement across this resistance was used to determine the current passing through it, and hence the EMAT coil, through the use of Ohm's law. For a supplied pulse with a rise time of 1 μs, the peak current amplitude is 1.75 kA per channel (see figure 3).

The driving circuit is similar to the driving electronics described by previous studies describing the development of a coil-only send-receive EMAT [32], but is capable of achieving much higher current amplitudes and hence more intense ultrasound generation, since the magnitude of the self-field Lorentz force scales with the square of the excitation current [29]. Even higher current amplitudes have been reported for a single coil using a spark-gap discharge driving circuit, although this is not as practical as a solid state switching method [23, 24, 32]. The solid state switching for each channel allows for accurate and reliable appli-

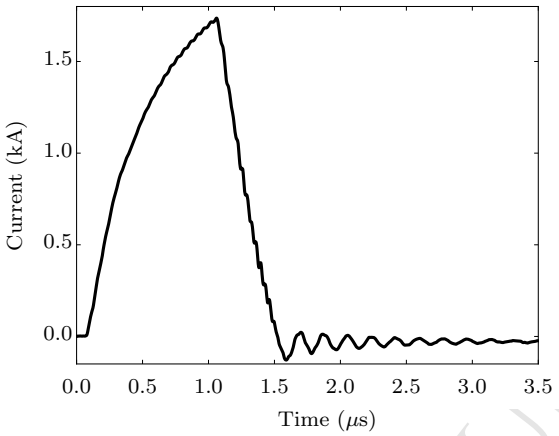

Figure 3: Excitation current pulse with a rise time of 1.0 μs and a peak value of approximately 1.75 kA. The current pulser system used to drive the EMAT array contains four channels capable of delivering these current pulses.

cation of phase delays, which is essential for control of the phased array beam characteristics.

3.2. Finite Element Analysis

The commercial software package PZFlex was used for all following finite element calculations. PZFlex implements an explicit time domain integration algorithm for solving dynamic elastic and acoustic fields. Further details relating specifically to the finite element solver can be found in reference [33].

3.2.1. Pulsed EMAT Array Optimisation

A high power EMAT pulser system consisting of four independent channels with programmable time delays was developed for EMAT array measurements on cast steel samples. Prior to the development of an experimental EMAT phased array transducer, finite element models were used to determine optimal array parameters. Compared to typical commercially available piezoelectric phased array systems, which are capable of driving up to 256 independent channels [31], the number of output channels available on the phased EMAT

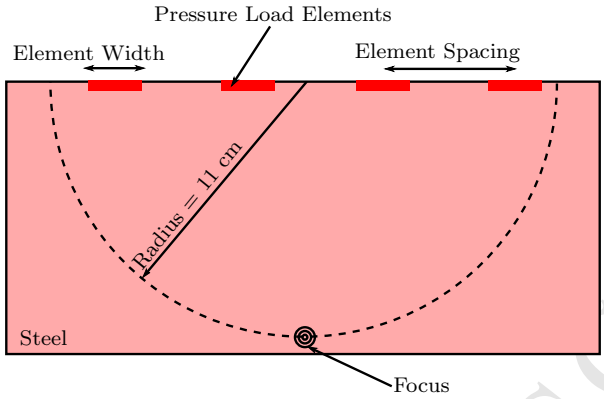

Figure 4: Schematic diagram of the finite element model geometry used for the optimisation study. EMAT elements were modeled by applying a spatially-uniform, temporally-varying pressure load on appropriate elements on the sample surface.

pulser's driving electronics is low. Typically when designing a phased array of any kind, it is beneficial to adhere to the diffraction limit and maintain an element separation equal to, or less than, a half-wavelength. With such a limited number of elements, however, the aperture would be small when adhering to the diffraction limit and hence the expected beam characteristics would be poor. Moreover, the inherent inefficiency of EMATs necessitates relatively large transducer footprints for practicable signal-to-noise ratios, making adherence to the diffraction limit difficult. A finite element study was therefore conducted to ascertain the best array parameters (element separation and element width) to achieve both a narrow beamwidth and sufficient sidelobe suppression.

Analysis of the self-field Lorentz generation mechanism indicates that the coil-only design can be approximated as a rectangular piston source [26]. Each EMAT element was therefore modeled by applying a uniform, time-varying, pressure profile across the relevant surface nodes in the model. Analytical modeling of the self-field mechanism indicates that the Lorentz force is proportional to the square of the driving current, leading to a doubling of the frequency content in the case of harmonic time dependence. The square of a half-cycle of a sine wave with a period of 2.0 μs was therefore chosen as the driving function for the pressure load in the model, to approximate the temporal pressure

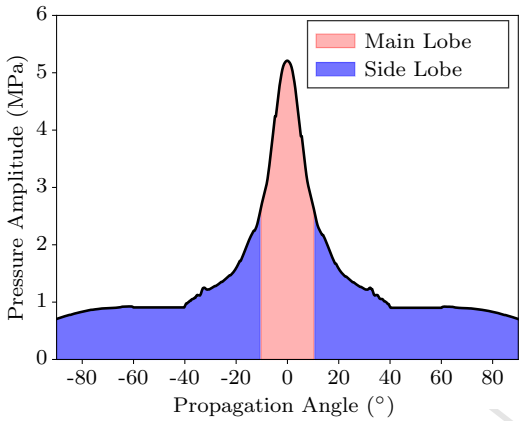

Figure 5: Example simulated beam profile data for a four-element array with element spacing 6 mm and element width 4 mm for a chosen focal point at a depth of 11 cm. The area shaded in red is within the 3 dB beam width. The blue area is outside of the 3 dB beam width and is where artifacts associated with non-conformance with the diffraction limit arise in the form of side and grating lobes.

variation supplied by a coil-only EMAT driven by the current profile shown in figure 3. A pressure amplitude of 40 MPa was selected as an order-of-magnitude approximation as determined from semi-analytical modeling.

The slowest expected bulk wave velocity in steel, the shear velocity, c_S, is approximately 3150 ms^{-1}, depending on the elastic constants of the sample being considered. The Fourier spectrum of the driving function indicates there is significant frequency content in the acoustic wave up to a frequency value, $f = 2$ MHz. In this model, the smallest expected wavelength of an ultrasound wave propagating in the bulk of the sample, $\lambda_m in$, is therefore approximately $\lambda_m in = c_S f^{-1} = 1.6$ mm. A finite element grid was meshed with an element density of 16 elements per wavelength in order to avoid numerical artifacts arising from coarse meshing relative to the wavelength [33].

Internal defects of interest in cast steel, such as segregation defects and associated cracking, are likely to lie along the centreline, which in a 22.5 cm thick slab is at a depth of approximately 11 cm below the sample surface [34, 35].

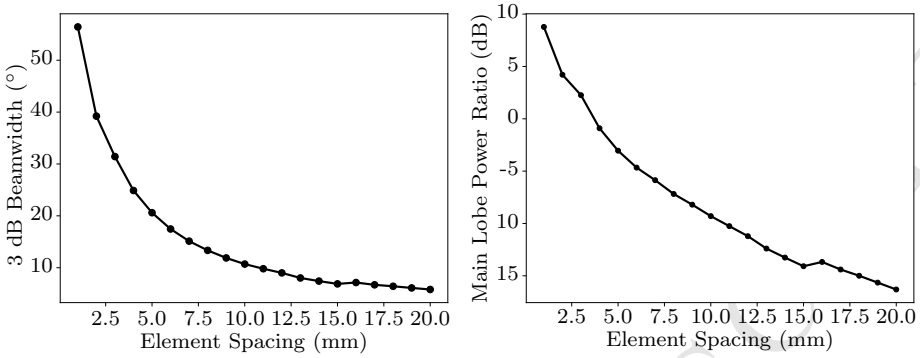

Figure 6: Modeled variation of the 3 db beamwidth (left) and main lobe to side lobe power ratio (right) with element spacing for a four-element phased array with 1 mm wide elements. As the array's aperture is increased, the beamwidth is reduced at the expense of increased signal content outside of the 3 dB beamwidth.

Phase delays were therefore applied in accordance with equation 3 to model the focusing of an incident longitudinal ultrasound pulse at a depth of 11 cm (see figure 4). The EMAT pulsing system available for experimental use has four channels, and so for meaningful comparison of the model with experimental results, a four-element EMAT generator was modeled in this way.

The EMAT generation array can be characterised in terms of two defining parameters; the element separation (the distance between the centre nodes of adjacent elements) and the element width (the width of the active element region). The aim of the study was to obtain the optimal values for these parameters to achieve a narrow beam width and high directivity in the generated beam.

A series of simulations were run in which the element width was kept constant at 1 mm and the element separation was varied between 1 and 20 mm. The model output was a two-dimensional grid of pressure history data for each node in the simulation. The beam profile was obtained by defining a semi-circle with radius 11 cm about the centre of the array and plotting the maximum absolute values from the pressure histories of the corresponding nodes as a function of angle from normal incidence. The beam profile was then parameterised in

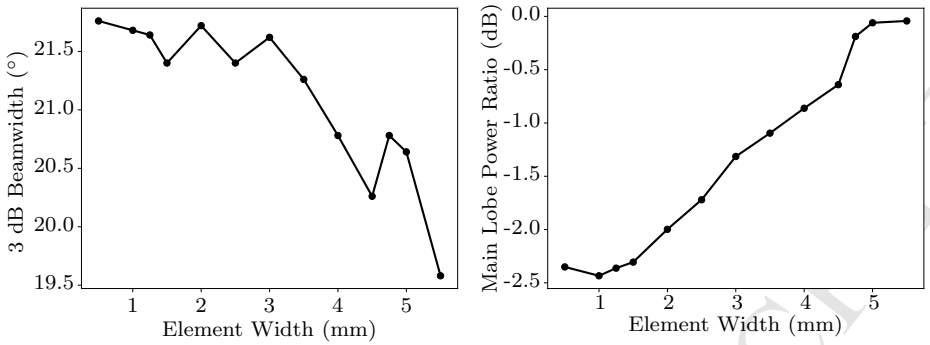

Figure 7: Modeled variation of the 3 db beamwidth (left) and main lobe to side lobe power ratio (right) with element width for a four-element phased array with an element spacing of 6 mm. The total variation in the beamwidth is quite small over the whole range of element widths, and the point-wise variation arises due to truncation errors associated with grid discretisation. Increasing the element width leads to a negligible effect on the beamwidth, whilst improving the main lobe power ratio.

terms of the 3 dB beam width (the angular range in which the beam amplitude is greater than, or equal to, half of the maximum amplitude, see figure 5) and in terms of the logarithmic ratio of integrated beam amplitude within the 3 dB beam width to integrated amplitude without of the 3 dB beam width. The first parameter serves as a metric for comparing the directivity of the main beam lobe; a narrower beam width gives a more localised high pressure region, which is beneficial when aiming to separate defect indications that lie laterally close to each other. The second parameter serves as an indication of the relative amplitude of side lobes; if the ratio is low, then more of the beam energy is directed outside of the main beam width and in separate lobes that are directed away from the intended target region, leading to regions of high localised amplitudes other than the intended focus, and therefore potentially confusing attempts at defect localisation using a focused beam.

The results from this series of simulations are displayed in figure 6. The overall observed trend is that an increased element separation reduces the 3 dB beam width, which is desirable, though at the expense of increasing power distributed through side lobes. This is to be expected; the larger array aperture

leads to a more well-defined focus, however since the number of elements in the array remains constant, each increase in aperture size moves the element separation further away from the diffraction limit and hence increasingly large side lobes are observed.

This can be to an extent mitigated by choosing a suitable element width. Figure 7 displays the beam characteristics modeled by choosing an array separation of 6 mm and varying the element width between 0.5 and 5.5 mm. It is observed that wider elements reduce side lobe generation for a marginal decrease in beam width. Intuitively, this can be explained through the consideration of each element as a normally-acting piston source. As the element width increases, proportionally more of the energy is directed downwards compared to a smaller element, for which contributions from the piston edge are proportionally greater and lead to non-normally-incident wave generation.

A full optimisation would require modeling array parameters throughout the two-dimensional parameter space, however it is clear from modeling with the fixed width and separation values that the choice of a large aperture with large elements leads to smaller beam widths with suppressed side lobes. The data in figure 6 show that large increases in element separation beyond 10 mm produce diminishing returns in terms of beam width, with the minimum achievable beamwidth being approximately 10 degrees. It was therefore decided that an EMAT array with element separation of 6 mm and with element widths of 4 mm provided a suitable compromise between narrow beam widths and suppressed side lobes. This choice of design gives a 3 dB beam width of 20 degrees, which corresponds to a lateral size of 8 cm in the centreline region (11 cm away from the transducer).

3.2.2. Phased Array Signal Enhancement

Using the optimised array parameters obtained in section 3.2.1, it is possible to determine the expected improvement in signal amplitude that results from phased array generation. A finite element model was constructed in which a four-element EMAT array on the upper surface of a 22.5 cm thick steel block

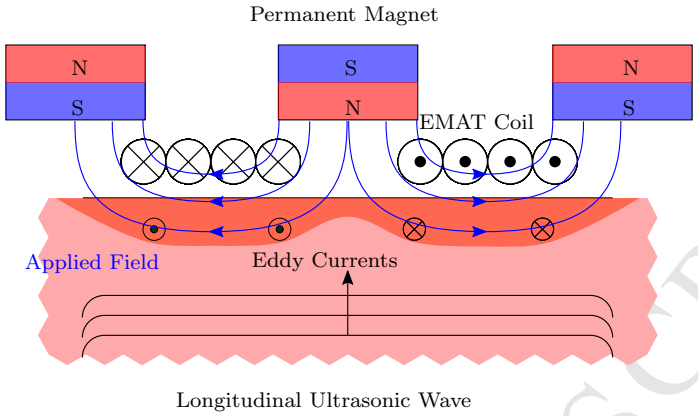

Figure 8: When an EMAT is used as a detection device, the oscillatory motion of the conducting sample's surface in the presence of a bias magnetic field generates eddy currents in the sample, which can be detected using an induction coil near the sample's surface. A bias magnetic field is always required when operating an EMAT as a detector, hence most designs utilise permanent magnets.

focused an incident longitudinal ultrasound pulse on the opposing surface directly underneath it. The driving function and mesh density were as described in section 3.2.1.

An EMAT detector is sensitive to surface particle velocity, and hence in order to model the signal as detected using an EMAT, the velocity vector history was recorded for each node in the simulation grid. Nodes on the lower surface were chosen which corresponded to an EMAT detector, with a footprint described by figure 10 (the geometry of the EMAT detectors used for experimental validation in this study), placed directly opposite the generation array. Out-of-plane velocity components in the bias field shown in figure 8 generate opposing eddy currents under each half of the detection coil (since the in-plane field has opposing polarities beneath each half of the coil), and hence out-of-plane particle velocities at surface nodes corresponding to the detection coil can be directly summed to obtain a proxy of the voltage signal as measured by the inductor coil. The out-of-plane bias field components do not have opposite polarities under each half of the coil, however, and so for a velocity vector that lies in the plane of the surface, unidirectional eddy currents are generated, leading to the

induced currents in the detection coil canceling each other. In-plane particle velocities at the coil surface nodes were therefore summed over each half of the coil and then subtracted to account for this cancellation effect.

The resulting values give a measure of the calculated relative amplitude of the expected EMAT signal, however the numbers are not directly comparable to experimental measurements without a full model of the EMAT detection device. This is an unnecessary complication due to the non-trivial field geometries arising from the permanent bias field and its interaction with the steel sample, the dependence of eddy current densities on sample properties and the degree of mutual inductance between the detection coil and the sample. Instead, it is sufficient to compare the difference in amplitude between similar models of a single EMAT element and a phased array to determine the expected signal enhancement from using the phased array approach.

The resulting velocity histories, summed over the appropriate nodes, are shown for the cases of a single EMAT generation element and generation by a phased array in figure 9. The difference in the peak-to-peak amplitude of the incident longitudinal pulse is a factor of 3.7. This result is to be expected, since it is approximately equal to the number of extra elements applied (though it is expected to be lower than 4, since attenuation losses at the focal point from the outer elements will be greater than for an element positioned directly above the focus, due to the increased path length).

3.3. EMAT detector design

A coil-only EMAT generator predominantly excites mechanical forces that lie out of the sample's surface plane, and hence lead primarily to longitudinal wave generation (see section 2.1). Efficient detection of these transmitted longitudinal signals therefore requires an EMAT design that is sensitive to out-of-plane particle motion, and hence requires a static bias field with significant in-plane components. This is relatively difficult to achieve, since the permanent magnet supplying the bias field must lie above the sample surface and because the in-plane magnetic flux density falls rapidly with distance from the magnet's

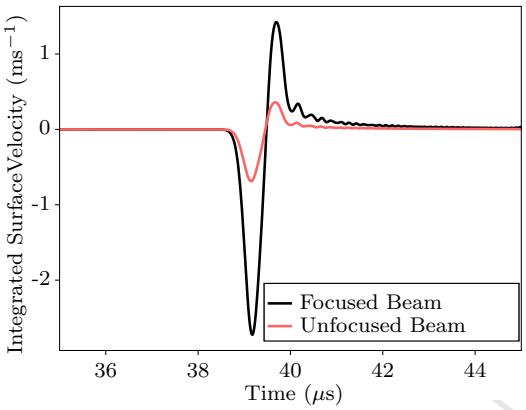

Figure 9: Finite element analysis demonstrates a factor of 3.7 improvement in the peak to peak amplitude of the transmitted longitudinal ultrasound signal from a four-element phased array when compared to a single element.

edge. Most longitudinal EMAT designs therefore involve winding an inductor coil around the edge of a permanent magnet, where there are significant parallel and perpendicular components to the field. Such a design leads to a large parasitic inductance in the coil, however, and the small area over which there are parallel field components leads to relatively weak received signals. For the application of bulk wave measurements in thick steel casts, it is important to optimise the detection EMATs, since the sample's thickness and high attenuation leads to small detectable signals.

Newer EMAT designs have considered the positioning of a flat spiral detection coil between magnets of alternating polarity [36] (see figure 8). The chief advantage of these designs is that they reduce the parasitic inductance in the coil and expose more of the coil's length to the sample, and so lead to more efficient detection of longitudinal ultrasound waves. Since the coils are still placed at the magnet edges, there is still in-plane particle motion sensitivity, and hence these designs are also suitable for detection of shear wave modes.

A longitudinal EMAT detector was constructed using $5 \times 10 \times 2.5$ mm NdFeB magnets. A 3D printed housing was used to hold three stacks of three such

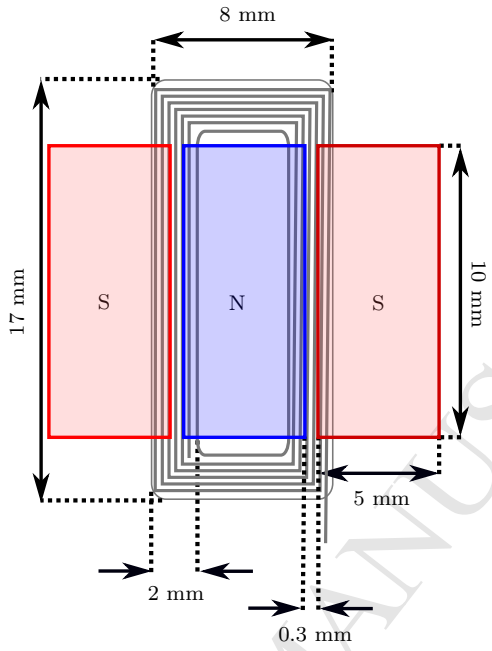

Figure 10: Schematic diagram depicting the coil dimensions of the detection sensor. Copper wire of 0.14 mm diameter was wound into kapton tape that was pressed into 3D printed coil templates with these dimensions. The magnets used in the detection sensor were NdFeB magnets with a height (out of the page) of 2.5mm, stacked three high. Separation gaps between the magnets ensure that in-plane static magnetic field components are large enough for out-of-plane particle displacement detection.

magnets with alternating polarities at a separation of 0.3 mm, and to align the inductor coil correctly in the resulting gaps between the magnets. Copper wire with a 0.14 mm diameter was used to wind a racetrack coil, with track width 3 mm, into the plastic template grooves beneath the magnets such that its edges lay under the magnet's edges. The coil was encased in kapton tape (see figure 10).

3.4. Experimental Validation of Signal Enhancement

Experimental validation of the amplitude enhancement observed in the finite element modeling was achieved using a four-element high power EMAT pulser and a series of EMAT generation coils wound into a 3D printed plastic template

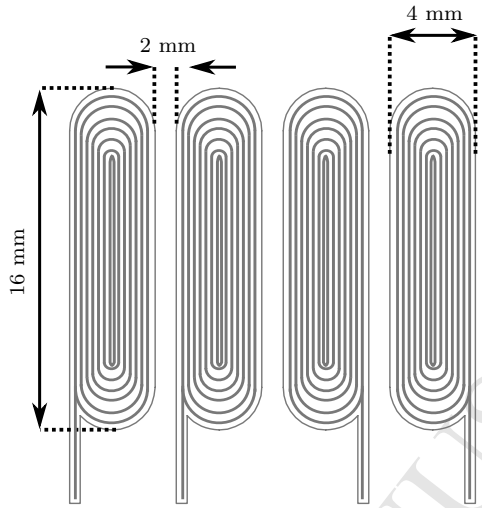

Figure 11: Schematic diagram depicting the coil dimensions of the generation array. Copper wire of 0.14 mm diameter was wound into kapton tape that was pressed into 3D printed coil templates with these dimensions.

to ensure tight control over element width and spacing. The EMAT array's generation coils were wound into a 3D printed template using 0.14 mm diameter copper wire enclosed in kapton tape. The parameters of the array (element spacing and width) were chosen on the basis of the finite element study presented in section 3.2.1, and so the width of each individual racetrack coil element was 4 mm, with the distance between the centres of adjacent elements being 6 mm (see figure 11).

Phase delays were applied in accordance with equation 3 to the four-element generation array to focus an incident pulse of longitudinal waves on the opposing face of a 22.5 cm thick as-cast steel slab sample. A single edge-field detection EMAT (constructed as described in section 3.3) was placed directly opposite; this was connected to an amplifier, which was then connected to an oscilloscope to measure the time-dependent voltage across the detection coil (see figure 12). An A-scan recording of the voltage history resulting from phased array generation was compared to the signal recorded when just a single generation element, placed directly opposite the detection coil, was fired (see figure 13). These mea-

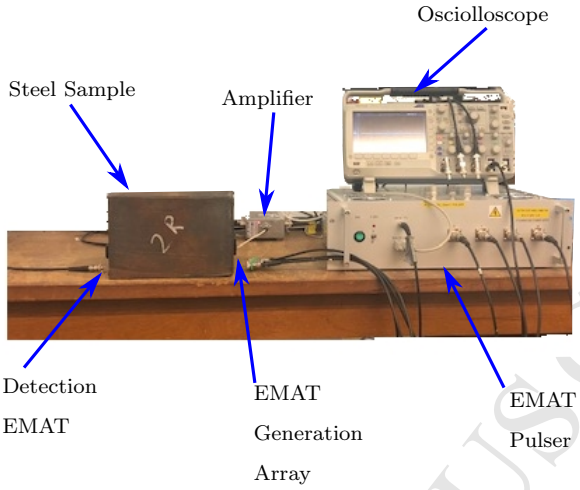

Figure 12: Schematic diagram of the experimental setup. The EMAT pulser (described in figure 2 drives the EMAT generation array (described in figure 11), which generates a focused longitudinal ultrasound wave. This is detected on the opposing side of the as-cast steel slab sample by the detection EMAT (described in figure 10). The signal is passed through an amplifier before being recorded on an oscilloscope.

surements were taken with no coherent averaging, but were digitally filtered using a Butterworth bandpass filter with low and high pass bands of 0.1 and 5.0 MHz respectively, and an order parameter of 1.

The received signals demonstrate a clear improvement in transmitted signal amplitude by a factor of approximately 3.5 when using a four-element phased array generator instead of a single EMAT. This figure is in good agreement with the expected enhancement by a factor of 3.7 determined from finite element analysis, as discussed in section 3.2.2.

3.5. Enhancement Using a Detection Array

The amplitude enhancement demonstrated by the use of a four-channel generation array can be further improved through the coherent addition of the transmitted signal as detected using an array of detection EMATs. Using the design outlined in section 3.3, an array of three detection EMATs was constructed with spacings of 3.0 cm between adjacent elements. The transmitted signal from the coil-only array generating at the opposite end of the sample

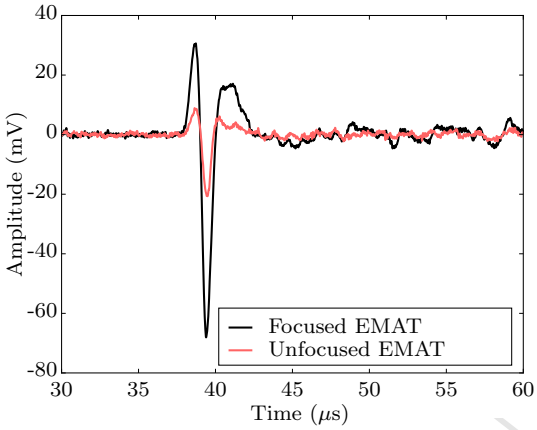

Figure 13: Experimental data demonstrating the enhancement of a longitudinal ultrasound signal transmitted through a 22.5 cm thick as-cast steel sample when using a four-element phased EMAT generation array. The signal amplitude is improved by a factor of 3.5 when compared to a single element, which is in good agreement with the factor of 3.7 improvement predicted by finite element analysis (see figure 9)

and focusing at a depth of 11 cm was recorded independently on each detection channel. The transmitted longitudinal pulse signal was identified in the A-scan trace recorded by the central element in the detection array and cross-correlated with the data from each channel to determine the phase separation of the signal as recorded by each element. These phase delays were then applied to the A-scan data from each channel, before summing to produce a single A-scan data set with enhanced amplitude in the longitudinal signal.

The principle of noise reduction through this delay-and-sum method is that any genuine ultrasonic signals arriving in the expected time intervals should be coherent and add constructively, whereas any noise due to stochastic processes should sum to zero if enough independent measurements are considered. This method therefore enhances ultrasound signals in the chosen time window and suppresses information which is not coherent between the independent measurements and is therefore likely composed of random noise. Assuming there are no physical differences between the signals detected by adjacent elements (ad-

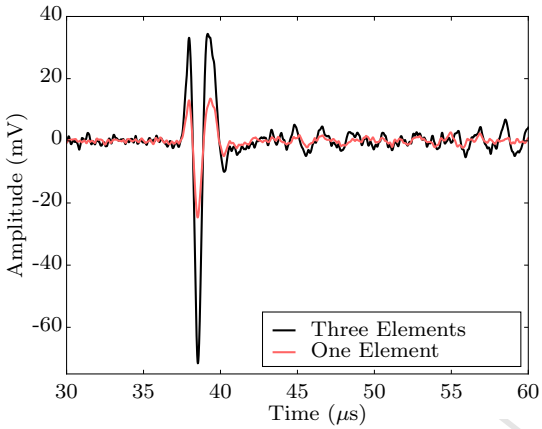

Figure 14: Comparison of the transmitted signals as received by a single EMAT detector and as received by three separate detectors after coherent summation. The improvement in the signal-to-noise ratio is 5.75 dB, which is comparable to the 4.77 dB improvement expected from the application of three coherent averages

ditional signals from defects or differences in the signal of interest, which arise due to the different spatial positions of the elements), the method is identical to the concept of coherent averaging, and thus is expected to improve the signal to noise ratio by a factor of $\sqrt{N}$, where N is the total number of elements used for detection and the signal and noise are parameterised in terms of their root mean square values [37].

The signal-to-noise ratio of an acoustic signal is here defined as 20 times the base 10 logarithm of the ratio of the sections of the A-scan trace that correspond to the signal of interest and which correspond to regions containing only noise, where no signals are expected:

$$SNR = 20\log_{10}\left(\frac{\sqrt{\frac{1}{n_{sig}}\sum_i S_i^2}}{\sqrt{\frac{1}{n_{noise}}\sum_i N_i^2}}\right), \tag{4}$$

where SNR is the value of the signal-to-noise ratio in decibels, n_{sig} and n_{noise} are the number of discrete values in the time series corresponding to the signal and noise sections of the data respectively and S_i and N_i are the i^{th} respective amplitude values of the signal and noise time series. In the A-scan data

presented in figure 14, the signal was defined as the transmitted longitudinal pulse recorded between 37.0 and 41.0 μs. The section of the A-scan trace beyond 41.0 μs was not considered for the signal-to-noise ratio comparison, since it isn't strictly composed only of stochastic noise; spurious scattered and mode-converted signals from grain structures in the sample would be expected to arrive after the main longitudinal pulse, and so the data in this region contain genuine acoustic signals that contain some information relating to the sample's grain structures. The noise was instead defined as the region between 15.0 and 35.0 μs, since it is physically impossible for acoustic signals from the generation source to be detected in this time window, and hence the data here represent genuine stochastic noise. The signal-to-noise ratio of the A-scans corresponding to the single detection element and to the coherent summation of signals from three detection elements (shown in figure 14) were calculated to be 25.67 dB and 31.42 dB respectively. The difference between these two values is 5.75 dB, which is comparable to the expected improvement due to coherent summation of 3 measurements ($20\log_{10}\left(\sqrt{3}\right) = 4.77$ dB), indicating both that the delay and summation method does improve the signal-to-noise ratio, and that it is identical to the coherent averaging method in the absence of spurious signals between elements.

4. Side-Drilled Hole Detection

With sufficient signal-to-noise ratio on detected ultrasound pulses propagated through the full thickness of a cast slab sample, it is possible to begin looking at detection experiments for internal defects. A four-element phased generation array was placed on the upper surface of a 32 cm thick steel sample with a 6 mm diameter side-drilled hole centred at a depth of 16 cm (see figure 15). Phase delays were applied in accordance with equation 3 to focus the incident longitudinal beam on the defect. A detection EMAT was placed adjacent to the generation array to record any backscattered ultrasound signals.

Close proximity of the detector coil to the high current generation devices

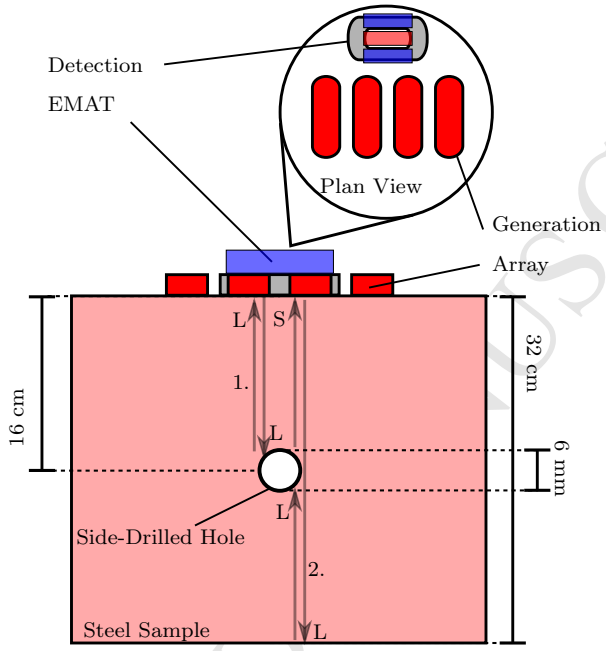

Figure 15: Schematic diagram of the pulse-echo experiment setup. The coil configuration shown was chosen to minimise exposure of the detection coil to magnetic flux from the generation coils and to minimise sensitivity to generated Rayleigh waves, which propagate perpendicular to the long axis of the coil. Path 1 corresponds to an incident longitudinal pulse (L) that is back-scattered at the defect. The total path length for path 1 is 31.4 cm and the longitudinal prpagation speed is approximately 5950 ms^{-1}, which leads to a signal arrival time of 52.8 μs. Path 2 corresponds to a longitudinal pulse that is reflected off the sample's backwall as a longitudinal wave before mode-converting to a shear wave (S) (due to tangential components to the displacement vectors at the defect's interface) and scattering forwards from the defect. The total propagation distance of the longitudinal mode in path 2 is 47.7 cm, and the shear mode travels 16.3 cm at a propagation speed of approximately 3150 ms^{-1}. The sum of the propagation times for these two path components leads to a signal arrival time of 132 μs. These defect indications are visible in figure 16, labelled b). and d). respectively.

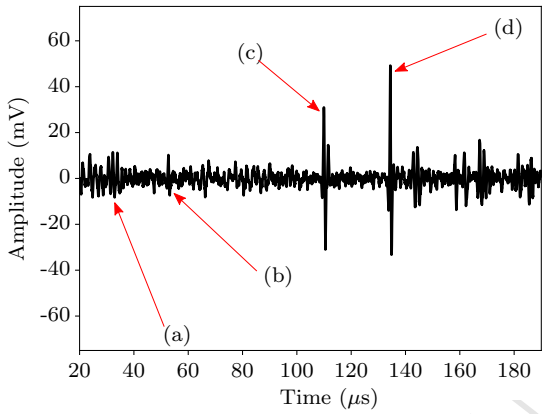

Figure 16: Pulse-echo A-scan data recorded on a 32 cm thick steel sample with a 6 mm diameter side-drilled hole at a depth of 16 cm (see figure 15). The received signals are interpreted as: (a), Rayleigh wave signals reflected from the sample edges at the surface, (b), back-scattered longitudinal wave from the defect, (c), reflected longitudinal wave from the sample's backwall, (d), reflected longitudinal wave from the back wall that has mode-converted at the defect and forward-scattered as a shear wave.

can saturate the amplifier and make detection of reflected ultrasound signals difficult. To an extent, this can be overcome through careful consideration of the relative positioning of the detection and generation coils. The generation elements used here are elongated, rounded rectangles or 'racetrack' shapes, and so the largest magnetic flux density during excitation occurs perpendicular to the long axis of the coil. Detection coils in close proximity exposed to this long axis become saturated during the excitation pulse. This effect can be mitigated by providing a suitable separation (3 cm) between parallel generation and detection coils, but this comes with the complication that the detection coils are aligned to efficiently detect Rayleigh waves, which mask signals arriving from the sample's interior. Instead, the coils can be aligned perpendicular to the generation array elements as shown in figure 15, which both exposes much less of the coil to the largest flux densities and so allows for smaller coil separations, and is a configuration that is less favourable for efficient detection of Rayleigh waves.

Using the coil arrangement described in figure 15, a pulse-echo ultrasound A-scan was recorded on the 32 cm thick steel sample (shown in figure 16). Although the chosen coil orientation prevents amplifier saturation, the close proximity of the detection coil to the generation coils gives a dead time of 20 μs. The data were therefore processed, firstly by windowing away the generation noise before 20 μs, before fitting the A-scan trace with a 7^{th} order polynomial and subtracting the fit function to de-trend the low frequency generation noise from the signal. High frequency noise was then removed using a Butterworth bandpass filter between 0.1 and 3.5 MHz. The small reflected signal at 53 μs (b) corresponds to a back-scattered longitudinal wave from the defect (corresponding to path 1 in figure 15). The larger pulses observed at 109 μs (c) and 132 μs (d) correspond to a longitudinal reflection off the sample's back wall and a forward-scattered mode-converted shear wave from the defect (corresponding to path 2 in figure 15) respectively. This interpretation of the A-scan trace in figure 16 has been corroborated with finite element analysis.

The results of this experiment suggest that for detection of small defects, the largest indications are provided by forward-scattered mode-converted signals. Although the sample used in this experiment is not as-cast, the signals in figure 16 that constitute the defect indication have traveled through 64 cm of steel, and so the prospect of detecting internal defects in a 22.5 cm thick as-cast slab sample remains promising.

5. Summary and Conclusions

This work has discussed the development of a compact, low cost, high current four-channel phased array EMAT pulsing system that can drive coil-only generation coils at currents in the range of 1.75 kA. The channels of this pulser system have programmable phase delays with a temporal resolution of 2.5 ns, which allows for focusing and steering of the generated ultrasound beam. Experiments performed on large (22.5 cm thick), coarse grained, as-cast steel slab samples with rough surfaces demonstrate an enhancement of the transmitted

signal by a factor of 3.5, and appropriate application of phase delays on three receiving elements can further improve the signal to noise ratio of a transmitted longitudinal signal by an additional factor of 1.9.

The EMAT phased array system presented in this work can deliver significant improvements in signal-to-noise ratio over the use of a single EMAT transducer. The ability to achieve high signal-to-noise ratio measurements in attenuative industrial cast steel samples using non-contacting sensors suitable for high-temperature application is a promising first step in the development of a measurement system that can be employed online during the continuous casting of steel for bulk and surface inspection of the slab. The experimental data presented here are supported by finite element calculations, indicating that such numerical simulation is appropriate for further development of the system.

Preliminary defect detection experiments have demonstrated that the high-power phased array system can be used to detect artificial void defects that are of similar size to the wavelength, although the highest-amplitude signals observed actually correspond to forward-scattered mode-converted shear waves instead of back-scattered longitudinal waves as is typical in a conventional pulse-echo arrangement. For measurement on as-cast samples, where signal amplitudes are expected to be lower due to poor surface condition and coarse grain structures, a transmission setup for detection of these mode-converted signals should be investigated. Although defect detection using the phased EMAT array has been demonstrated, further studies are required to demonstrate defect detection in as-cast samples, and in particular to demonstrate detection of real casting defects in industrial samples.

6. Acknowledgments

The author would like to thank the EPSRC and Tata Steel for funding this research.

7. References

[1] J. Sirgo, R. Campo, A. Lopez, A. Diaz, L. Sancho, Measurement of centerline segregation in steel slabs, Industry Applications Conference, 2006. 41st IAS Annual Meeting. Conference Record of the 2006 IEEE 1 (2006) 516–520.

[2] F. Boue-Bigne, Laser-induced breakdown spectroscopy applications in the steel industry: Rapid analysis of segregation and decarburization, Spectrochim. Acta, Part B.

[3] H. Presslinger, et al., Methods for assessment of slab centre segregation as a tool to control slab continuous casting with soft reduction, ISIJ Int. 46 (12) (2006) 1845–1851.

[4] N. Neogi, D. Mohanata, P. Dutta, Review of vision-based steel surface inspection systems, EURASIP Journal on Image and Video Processing 50.

[5] M. Reger, V. Balazs, R. Josza, Control of centerline segregation in slab casting, Acta Polytechnica Hungarica 11 (4) (2014) 119–137.

[6] G. Goode, R. Lewis, A momentary-contact system for ultrasonic testing of steel at temperatures up to i 200c, Non-Destructive Testing (1975) 313.

[7] G. Canella, F. Monti, Ultrasonic inspection of hot thick steel products, NDT Int. (1980) 10.

[8] I. Baillie, P. Grifith, S. Dixon, Implementing an ultrasonic inspection system to find surface and internal defects in hot, moving steel using emats, Insight 49 (2) (2007) 87–92.

[9] X. Jian, I. Baillie, S. Dixon, Steel billet inspection using laser-emat system, J. Phys. D: Appl. Phys. 40 (2007) 1501–1506.

[10] C. Scruby, B. Moss, Non-contact ultrasonic measurements on steel elevated temperatures, NDT and E Int. 26 (4) (1993) 177188.

[11] E. Papadakis, L. Lynnworth, K. A. Fowler, E. H. Carnevale, Ultrasonic attenuation and velocity in hot specimens by the momentary contact method with pressure coupling, and some results on steel to 1200 c, J. Acoust. Soc. Am 52 (1972) 850.

[12] K. Whittington, Ultrasonic testing at high temperatures, Phys. Technol. 9 (1978) 62.

[13] S. Davies, C. Edwards, G. Taylor, S. Palmer, Laser-generated ultrasound: its properties, mechanisms and multifarious applications, J. Phys. D: Appl. Phys. 26 (1993) 329–348.

[14] W. Grandia, Nde applications of air-coupled ultrasonic transducers, IEEE Ultrasonics Symposium (1995) 697–709.

[15] W. Deutsch, Automated ultrasonic inspection, WCNDT Conference 47 E (1) (2000) 1.

[16] L. Beaujard, Rev de Metall 62 (1965) 1187–1191.

[17] X. Jian, S. Dixon, Enhancement of emat and eddy current using a ferrite back-plate, Sens. Actuators, A 136 (2007) 132–136.

[18] M. Sgarbi, V. Colla, S. Cateni, S. Higson, Pre-processing of data coming from a laser-emat system for non-destructive testing of steel slabs, ISA Trans. 51 (2012) 181.

[19] R. Dewhurst, Q. Shan, Optical remote measurement of ultrasound, Meas. Sci. Technol. 10 (1999) R139R168.

[20] X. Jian, I. Baillie, S. Dixon, Steel billet inspection using laser-emat system, J. Phys. D: Appl. Phys. 40 (2007) 1501–1506.

[21] T. Takishita, K. Ashida, N. Nakamura, H. Ogi, M. Hirao, Development of shear-vertical-wave point-focusing electromagnetic acoustic transducer, Jpn. J. Appl. Phys 54 (2015) 07HC04.

[22] C. Thring, Y. Fan, R. Edwards, Focused rayleigh wave emat for characterisation of surface-breaking defects, NDT&E International 81 (2016) 20–27.

[23] D. Rueter, T. Morgenstern, Ultrasound generation with high power and coil only emat concepts, Ultrasonics 54 (2014) 2141–2150.

[24] D. Rueter, Induction coil as a non-contacting ultrasound transmitter and detector: Modeling of magnetic fields for improving the performance, Ultrasonics 65 (2016) 200–2010.

[25] X. Jian, S. Dixon, R. Edwards, J. Morrison, Coupling mechanism of an emat, Ultrsonics 44 (2006) 653–656.

[26] X. Jian, S. Dixon, K. Grattan, R. Edwards, A model for pulsed rayleigh wave and optimal emat design, Sens. Actuators, A 128 (2006) 296.

[27] H. Wheeler, Formulas for the skin effect, Proc. IRE 30 (9) (1942) 412.

[28] C. Dodd, W. Deeds, Analytical solutions to eddy-current probe-coil problems, J. Appl. Phys. 39 (6) (1968) 2829.

[29] M. Hirao, H. Ogi, EMATs for Science and Industry, Springer Science and Business Media, 2003.

[30] H. Ogi, M. Hirao, Line-focusing of ultrasonic sv wave by electromagnetic acoustic transducer, J. Acoust. Soc. Am. 103 (1998) 2411.

[31] B. Drinkwater, P. Wilcox, Ultrasonic arrays for non-destructive evaluation: A review, NDT&E International 39 (2006) 525–541.

[32] D. Rueter, Experimental demonstration and circuitry for a very compact coil-only pulse echo emat, Sensors 17 (2017) 926.

[33] G. Wojcik, D. Vaughan, N. Abboud, J. Mould Jr., Electromechanical modeling using explicit time-domain finite elements, IEEE Ultrasonics Symposium Proceedings (1993) 1107–1112.

[34] N. Pradhan, N. Banerjee, B. B. Reddy, S. Sahay, D. S. Basu, P. Bhor, S. Das, S. Bhattyacharya, Control of defects during continuous casting of line pipe (api) quality steels, Scand. J. Metall. 34 (2005) 232–240.

[35] D. Bhattacharya, T. Roy, V. V. Mahashabde, A study to establish correlation between intercolumnar cracks in slabs and off-center defects in hot-rolled products, J. Fail. Anal. Prev. 16 (2016) 95–103.

[36] M. da Cunha, J. Jordan, Improved longitudinal emat transducer for elastic constant extraction, Frequency Control Symposium and Exposition, 2005. Proceedings of the 2005 IEEE International (2005) 426.

[37] O. Rompelman, H. Ros, Coherent averaging technique: A tutorial review, J. Biomed. Eng. 8 (1986) 24.